Syddansk Universitet

Advances in Photonics Design and Modeling for Nano- and Bio-photonics Applications

Tanev, Stoyan

DOI:
10.1117/12.881624

Publication date:
2010

Document Version
Final published version

Link to publication

Citation for pulished version (APA):
Tanev, S. (2010). Advances in Photonics Design and Modeling for Nano- and Bio-photonics Applications. DOI: 10.1117/12.881624

Advances in Photonics Design and Modeling
for Nano- and Bio-photonics Applications

Stoyan Tanev,[* 1] Valery Tuchin,[2,3] Pavel Cheben,[4] Przemek Bock,[4] Jens Schmid,[4] and James Pond[5]

Integrative Innovation Management Unit, Department of Industrial and Civil Engineering
University of Southern Denmark, Niels Bohrs Alle 1, DK-5230 Odense M, Denmark
[2] Institute of Optics and Biophotonics, Saratov State University, Saratov, 410012 Russia
[3] Institute of Precise Mechanics and Control of RAS, Saratov 410028, Russia
[4] Institute for Microstructural Sciences, National Research Council Canada, Ottawa, Canada
[5] Lumerical Solutions, Inc., Vancouver, BC, Canada

ABSTRACT

In this invited paper we focus on the discussion of two recent unique applications of the Finite-Difference Time-Domain (FDTD) simulation method to the design and modeling of advanced nano- and bio-photonic problems. We will first discuss the application of a traditional formulation of the FDTD approach to the modeling of sub-wavelength photonics structures. Next, a modified total/scattered field FDTD approach will be applied to the modeling of biophotonics applications including Optical Phase Contrast Microscope (OPCM) imaging of cells containing gold nanoparticles (NPs) as well as its potential application as a modality for *in vivo* flow cytometry configurations. The discussion of the results shows that the specifics of optical wave phenomena at the nano-scale opens the opportunity for the FDTD approach to address new application areas with a significant research potential.

Keywords: Finite-difference time-domain method, sub-wavelength nanophotonic structures, optical phase contrast microscope, optical clearing effect, biological cell, gold nanoparticles, biomedical imaging

1. INTRODUCTION

The study of optical wave phenomena at the nano-scale requires the application of rigorous numerical electrodynamics modeling. In most cases optical simulations could be the only way to get a deeper understanding of light propagation and scattering in advanced nanopotonic structures. The situation is very similar in nanobiophotonics diagnostics and imaging research studies where the optical scattering phenomena are initiated at a comparable scale of dimensions. This similarity enables a common way of treatment with respect to the challenges associated with numerical modeling of optical wave phenomena at the nano-scale. The tools and methods for the numerical modeling of light scattering from single or multiple biological cells are of particular interest since they could provide information about the fundamental light-cell interaction phenomena that is highly relevant for the practical interpretation of cell images by pathologists. The FDTD simulation and modeling of the light interaction with single and multiple, normal and pathological biological cells and sub-cellular structures has attracted the attention of researchers since 1996.[1] The emerging relevance of nanobiophotonics imaging research has established the FDTD method as one of the powerful tools for studying the nature of light-cell interactions. The main advantages of the FDTD method are: i) its numerical simplicity and straightforward physical basis since it is a numerical solution of Maxwell's equations, and ii) its ability to be easily integrated with a graphical user interface enabling its broader adoption as a research tool. This paper will focus on summarizing some recent advanced applications of the FDTD approach to the modeling of i) Subwavelength Grating Structures (SWG) for refractive index engineering in microphotonic silicon waveguides,[2,3] and ii) Optical Phase Contrast Microscope (OPCM) imaging of cells containing gold nanoparticles (NPs).[4-6] The focus will be on the simulation results and the design and modeling power of the FDTD approach rather than on the specific mathematical formulation. Details about the numerical aspects of the FDTD can be found elsewhere.[7]

[*] tan@ib.sdu.dk

2. SWG STRUCTURES FOR REFRACTIVE INDEX ENGINEERING IN MICROPHOTONIC SILICON WAVEGUIDE CROSSINGS

This section focuses on the numerical modeling of a recent experimental demonstration of using SWG structures for refractive index engineering in microphotonic silicon waveguide crossings by the Optoelectronics Group in the Institute for Microstructural Sciences at the National Research Council in Ottawa, Ontario, Canada. The SWG design exploits the effective medium principle, which states that different optical materials, combined at subwavelength scales, can be approximated by an effective homogeneous material.[8,9] Within this approximation, an effective medium can be characterized by an effective refractive index defined by a power series of the homogenization parameter $\chi = \Lambda / \lambda$, where Λ is the grating pitch and λ is the wavelength of light. Provided that the pitch Λ is less than the 1st order Bragg period $\Lambda_{Bragg} = \lambda /(2n_{eff})$, the grating operates in a subwavelength regime and the diffraction effects are frustrated. An example of a basic structure that exemplifies the use of refractive index engineering in a waveguide is shown in Fig. 1a.[2] It is a nonresonant photonic structure formed by etching a linear periodic array of rectangular segments into a 260-nm-thick single crystal silicon layer of a silicon-on-insulator wafer. A 2-μm-thick bottom oxide (SiO_2) layer separates the waveguide from the underlying silicon substrate. The waveguide core is a composite medium formed by interlacing the high-refractive-index segments with a material of a lower refractive index, which at the same time is used as the cladding material. The refractive index of the core is controlled lithographically by changing the volume fractions of the two materials. By intermixing Si and SU-8 materials at the subwavelength scale, the refractive index range of ~1.6-3.5 can be obtained. In order to avoid the formation of standing waves due to Bragg scattering and the opening of a band gap near 1550 nm wavelength, a nominal structural period d = 300 nm was chosen, which is less than a half of the effective wavelength of the waveguide mode λ_{eff}. Fig. 1b shows the dispersion diagrams of the periodic SWG waveguide and of an equivalent strip waveguide with a core index of 2.65.[2] The comparison of the two dispersion curves shows that the dispersion away from the bandgap resonance matches that of an equivalent strip waveguide.
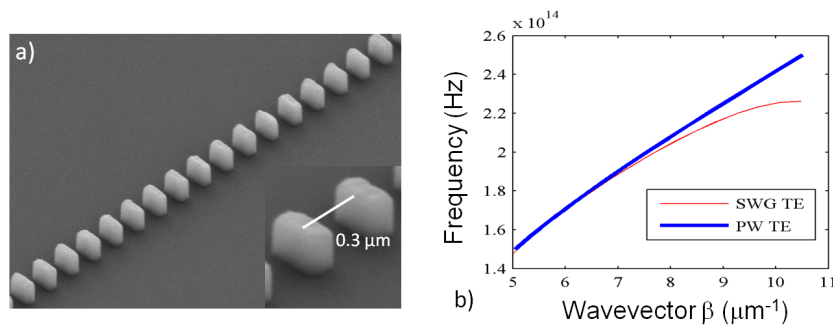

Fig. 1. a) SWG waveguide (SEM image); b) Dispersion diagrams for SWG and an equivalent strip waveguide with an engineered core refractive index of 2.65 (TE polarization).

In the case of SOI waveguide platforms, the two natural choices for the high and low index materials to create the effective medium are silicon (waveguide core) and silica (cladding) respectively. A gradual change in the ratio of Si to SiO_2 along the light propagation direction will result in a corresponding effective refractive index change of the composite medium of the waveguide core. This effect can be sued to design a SWG mode converter for efficient waveguide crossings. This is done by gradually changing the effective index of the SWG waveguide through chirping the pitch and tapering the width of the grating segments (Fig. 2).[3] Reducing the segment width as the mode propagates along the crossing expands the mode near the crossover point. Since the SWG waveguide intersecting this expanded mode is also subwavelength, diffraction is frustrated resulting in minimal loss. At the same time coupling to the intersecting waveguide is reduced.[3]

The usual total field/scattered filed approach was used to perform 3D FDTD simulations with a mesh size of $10\times20\times10$ nm^3 to ensure finer resolution for the taper and chirp (in the direction of the x- and z-coordinates, respectively, as shown in Fig. 2a).[3] The increased numerical accuracy is at the expense of layout size, which is $3\times3\times10\mu m^3$. The values of the refractive indices of the materials that were used are 3.476 for Si and 1.444 for SiO_2, the time step is 1.67×10^{-17}s in accordance with the Courant criterion.[7] The simulation layout for a Si wire waveguide with a SWG crossing is the one shown in Fig. 2a, where Λ_i and Λ_f are the initial and final grating pitches, w_i and w_f are the initial and final segment widths, $a = 150$ nm is the segment length, and $h = 260$ nm is the Si thickness in the SOI wafer.[3]
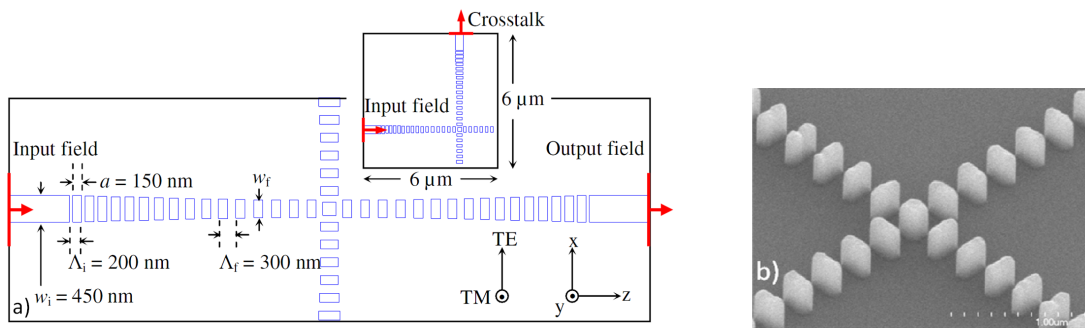
Fig. 2. a) Top view of the 3D FDTD simulation layout for a Si wire waveguide with a SWG crossing, where Λ_i and Λ_f are the initial and final grating pitches, w_i and w_f are the initial and final segment widths and $a = 150$ nm is the segment length. Inset in (a) shows the layout for estimating crosstalk. b) Example of a micro-fabricated waveguide crossing.

This layout was used to calculate loss, whereas the layout inset in Fig. 2a was used to calculate crosstalk. A continuous wave (CW) fundamental mode of a 450nm× 260nm wire waveguide at $\lambda = 1.55$ μm is used as the input field and optimization is performed for TE polarization. Mode mismatch loss is calculated as the power coupled to the fundamental mode of the output wire waveguide, whereas crosstalk is calculated as the power coupled to the fundamental mode of the intersecting waveguide. To reduce the mode mismatch loss from a wire waveguide to SWG in Fig. 2a, we ensure an adiabatic transition by a linear chirp (from $\Lambda_i = 200$nm to $\Lambda_f = 300$nm) and taper (from $w_i = 450$ nm to w_f in the range of 200nm-350nm) over 12 grating segments. The taper section is followed by 8 SWG segments with a constant pitch of 300nm and a width of 300nm (with a=150nm, i.e., a constant duty cycle of 50 %). The intersecting SWG structure has the same grating parameters, while the center segment is square to ensure an identical geometry for both waveguides. For each w_f, the center segment dimensions are set to match the area of the adjacent SWG grating segment ($w_f \times a$) ensuring a constant effective index for these adjacent segments. After the crossing point, an identical geometry is used for transition back to a wire waveguide (Fig. 2a).[3]
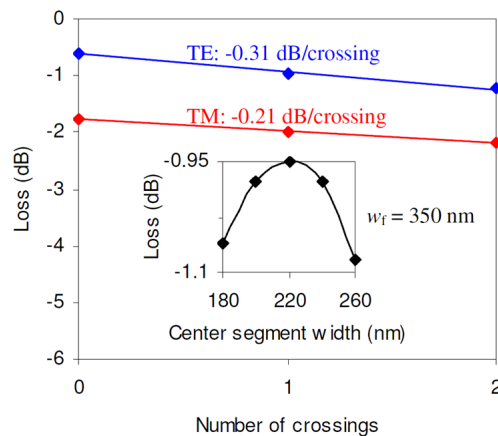

Fig. 3. SWG loss per crossing for TE (blue) and TM (red) polarizations for w_f = 350 nm. The inset shows loss for one SWG crossing with varying center square segment width w.

To determine loss per SWG crossing in the simulations (Fig. 3) w_f = 350 nm was used to minimize taper insertion loss. Loss per crossing is calculated as the slope of the linear fit to the insertion loss from three structures, comprising 0, 1 and 2 crossings. Fig. 3 shows that for TE polarization the loss is -0.31 dB/crossing, while for TM polarization the loss is -0.21 dB/crossing. The inset in Fig. 3 shows one SWG crossing loss (w_f=350nm) for different widths of the center square segment indicating optimal performance at w = 220nm.

This example demonstrates the application of the FDTD approach for the design and modeling of a new waveguide crossing principle based on subwavelength grating waveguides. The fabrication of such micro-waveguide structures is

impossible without the preliminary design and modeling step that was based on the application of the FDTD approach. The new device was experimentally fabricated.[3] The measured loss of the fabricated structures is as low as -0.023 dB/crossing, polarization dependent loss is minimal (0.01 dB) and crosstalk is less than -40 dB. An important advantage of this SWG structure is that it can be fabricated with a single etch step. Subwavelength grating crossings have the potential to facilitate massive interconnectivity and minimize the device footprint for future complex planar waveguide circuits.

3.   THE FDTD OPCM APPROACH

The 3D FDTD formulation provided in this section is based on a modified version[4-6] of total-field/scattered-field (TFSF) FDTD formulation.[7] It could be more appropriately called total-field/reflected-field (TFRF) formulation. The 3D TFRF formulation uses a TFSF region which contains the biological cell and extends beyond the limits of the simulation domain. The extension of the transverse dimension of the input field beyond the limits of the computational domain through the perfectly matched boundaries would lead to distortions of its ideal plane wave shape and eventually distort the simulation results. To avoid these distortions one must use Bloch periodic boundary conditions (Fig. 4ab) in the lateral x - and y -directions which are perpendicular to the direction of propagation $- z$.[4-6]

Phase contrast microscopy produces high-contrast images of transparent specimens such as living cells and sub-cellular components. In a conventional flow cytometry configuration a beam of light of a single wavelength is directed onto a hydro-dynamically focused stream of fluid driving a periodical array of cells to flow through it. The OPCM simulation model requires the explicit availability of the forward scattered transverse distribution of the fields. The phase of the scattered field accumulated by a plane wave propagating through a biological cell within a cytometric cell flow will be used in the FDTD model of the OPCM that is described as the follows.
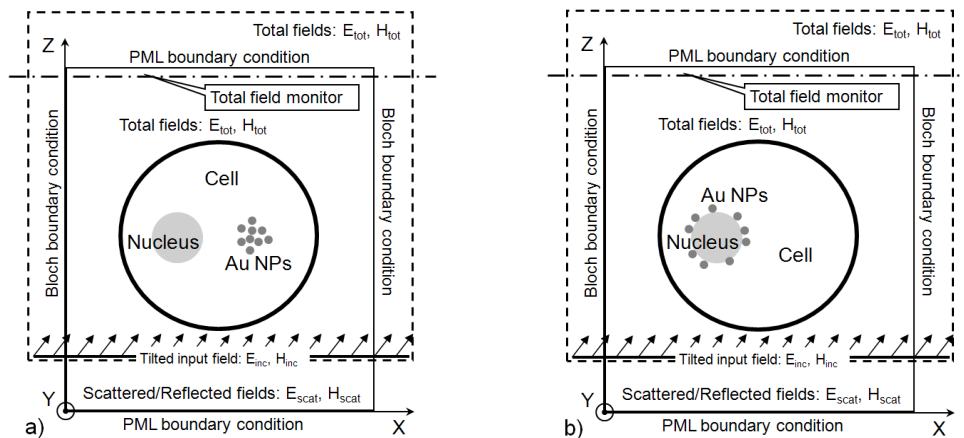

Fig. 4. Schematic representation of the 3D FDTD formulation including: a) a cell with a nucleus and a cluster of gold nanoparticles in the cytoplasm; b) a cell with gold nanoparticles randomly distributed on the nucleus surface.

Fig. 5ab shows a flow cytometry configuration of a phase contrast microscope, where an image with a strong image contrast ratio is created by coherently interfering a reference (R) with a beam (D) that is diffracted from one particular cell in the cell flow. The phase contrast microscope uses incoherent annular illumination that could be approximately modeled by adding up the results of eight different simulation using ideal input plane waves incident at a given polar angle (30 deg), an azimuthal angle (0, 90, 180 or 270 deg), and a specific light polarization (parallel or perpendicular to the plane of the graph).

Every single FDTD simulation provides the near field components in a transverse monitoring plane located right behind the cell (see Fig. 4ab). The far field transformations use the calculated near fields right behind the cell and return the three complex components of the electromagnetic fields far enough from the location of the near fields, i.e. in the far field.[7] The amplitudes and the phases of the calculated far-field components can be used then to do Fourier optics with both the scattered and reference beams.
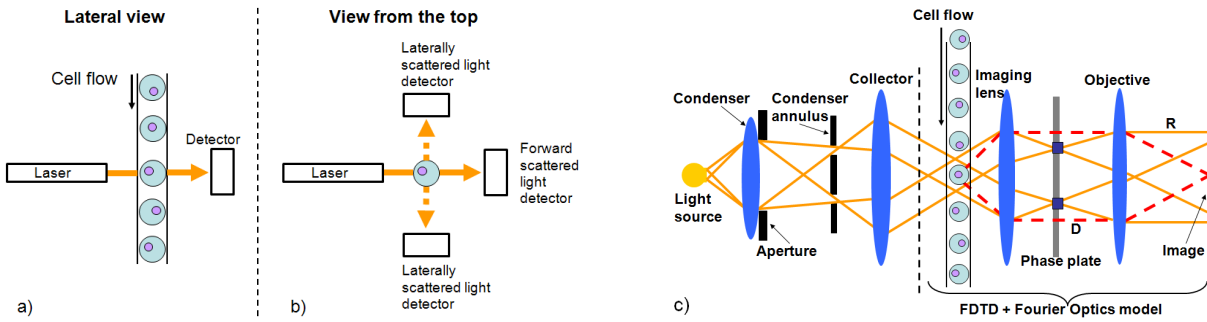
Fig 5. OPCM cytometer (a,b) with a visual representation of the FDTD OPCM model (c) including the propagation of the reference (R) beam without the cell flow and the propagation of the beam diffracted (D) from one of the cells.

The magnification factor of the optical lens system was implemented by merely modifying the angle of light propagation – it was applied to the far fields before the interference of the diffracted (D) and reference (R) beams (Fig. 5c) at the image plane.[4-6] The effect of the numerical aperture NA is to clip any light that has too steep an angle and would not be collected by the lens system. The OPCM images at the image plane are calculated by adding up the scattered and the reference beam at any desired phase offset Ψ. To model the resonant and non-resonant scattering and absorption properties of the gold nanoparticles (NPs) we used the dispersion model for gold derived from the experimental data provided by Johnson and Christy.[10] The FDTD technique was applied to calculate the extinction cross-sections over a 400-900 nm wavelength range for a single 50 nm diameter gold NPs immersed in a material having the properties of the cytoplasm ($n_{cyto} = 1.36$) and space resolution $10 nm$. The calculated extinction cross-section has a maximum of 3.89 at 543.0 nm corresponding to one of the radiation wavelengths of He-Ne lasers. The result for $\lambda = 676.4 nm$ (a Krypton laser wavelength) which corresponds to the non-resonant case (extinction cross-section value 0.322, ~12 times smaller than 3.89). The FDTD results were validated by comparing them with the theoretical curve calculated by Mie theory.

4. FDTD OPCM SIMULATION RESULTS

The 3D FDTD modeling of OPCM imaging of single biological cells uses optical magnification factor $M = 10$ and numerical aperture $NA = 0.8$. The cell is modeled as a sphere with a radius $R_c = 5 \mu m$ (Fig. 1) with membrane thickness $d = 20 nm$. It corresponds to an effective (numerical) thickness of approximately 10 nm. The cell nucleus is also spherical with a radius $R_n = 1.5 \mu m$ centered at a position 2.0 μm away from the cell center in a direction perpendicular to the direction of light propagation. The refractive index of the cytoplasm is $n_{cyto} = 1.36$, $n_{nuc} = 1.4$ of the nucleus, $n_{mem} = 1.47$ of the membrane and $n_{ext} = 1.33$ of the extra-cellular material (no refractive index matching). The case of $n_{ext} = 1.36$ corresponds to refractive index matching (RIM) which through optical clearing ensures a better contrast of the cell image.[11] Fig. 4a shows the schematic positioning of a cluster of 42 NPs in the cytoplasm that was used in simulations. The cell center is located in the middle ($x = y = z = 0$) of the computational domain with dimensions $15 \mu m \times 12 \mu m \times 15 \mu m$ (Fig. 1a). The nucleus' center is located at $x = -2 \mu m$, $y = z = 0 \mu m$. The cluster of gold NPs is located at $x = 2 \mu m$, $y = z = 0 \mu m$. Fig. 4b shows another simulation scenario where the cluster of 42 NPs is randomly distributed on the surface of the cell nucleus. One of the main goals of this section is to illustrate the ability of the FDTD approach to model generate OPCM cell images including the imaging effects of optical clearing and gold NP resonance. The presence of NPs at non-resonant regime ($\lambda = 676.4 nm$) can be clearly seen on the graph shown in Fig. 6 (left). It represents a comparison of the cross-sections of two cell images – one with the cluster of NPs and one without it.
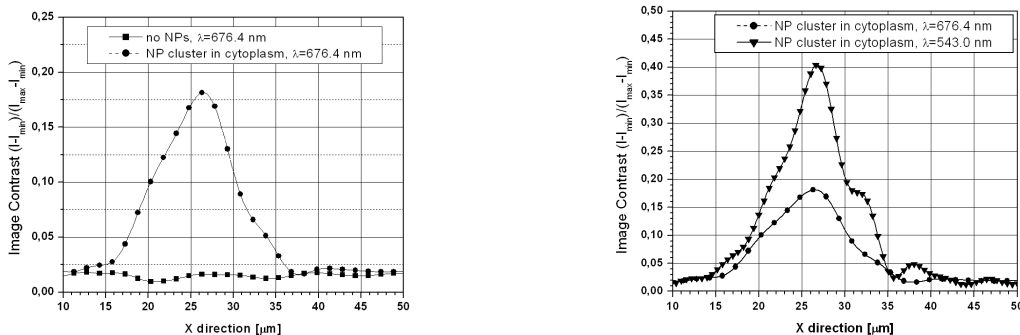
Fig. 6. Left: Comparison of the geometrical cross sections of two OPCM images – with and without nanoparticles ($\lambda = 676.4\text{nm}$, $\Psi = 180^\circ$). The non-resonant effect of the presence of the gold NPs is clearly visible. Right: Comparison of the geometrical cross sections of two OPCM cell images with gold NPs at resonant and non-resonant conditions ($\Psi = 180^\circ$). The effect of the optical resonance ($\lambda = 543.0\text{nm}$ vs $\lambda = 676.4\text{nm}$) of the gold NPs is clearly demonstrated
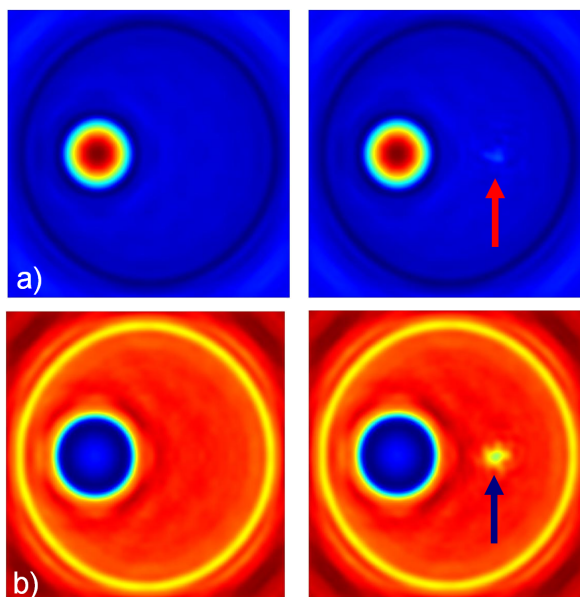

Fig. 7. OPCM images of a single cell for different values of Ψ (a: -150°, b: -90°) at RIM conditions with (right) and without (left) a cluster of 42 gold NPs at non-resonant conditions ($\lambda = 676.4\text{nm}$). The arrows indicate the position of the cluster.

The full images of the cell are shown in Fig. 7 for two different values of the phase offset Ψ between the reference beam and the scattered beam. The images demonstrate that the value of the phase offset Ψ affects the image contrast and needs to be optimized during real life experiments. The effect of the optical resonance of the gold NPs can be clearly seen in Fig. 6 (Right) - for $\Psi = 180^\circ$ when the resonant optical contrast of the gold NP peak is ~2.24 times larger than the non-resonant one. It however needs to be studied as a function of the particular phase offset Ψ between the reference beam and the scattered beam of the OPCM. An additional analysis of the optical contrast due to the gold NP cluster as a function of the phase offset showed that the enhancement of the optical contrast due to the NP resonance changes significantly from a minimum of 0.0 ($\Psi = 0^\circ$) to a maximum of 3.60 ($\Psi = -150^\circ$). This dependence could be important in real life OPCM imaging. The full images of the cell are shown in Fig. 8 for two different values of the phase offset Ψ between the reference beam and the scattered beam. The images illustrate the optical contrast effect of the optical resonance of the gold NPs. Fig. 9 shows the OPCM images of a cell including a group of 42 gold NPs randomly distributed on the surface of the cell nucleus at and non-resonant (left) and resonant (right) conditions. The optical wave phenomena involved in this second simulation scenario are fundamentally different from the ones considered earlier where the gold NPs are randomly distributed within the homogeneous material of the cytoplasm.
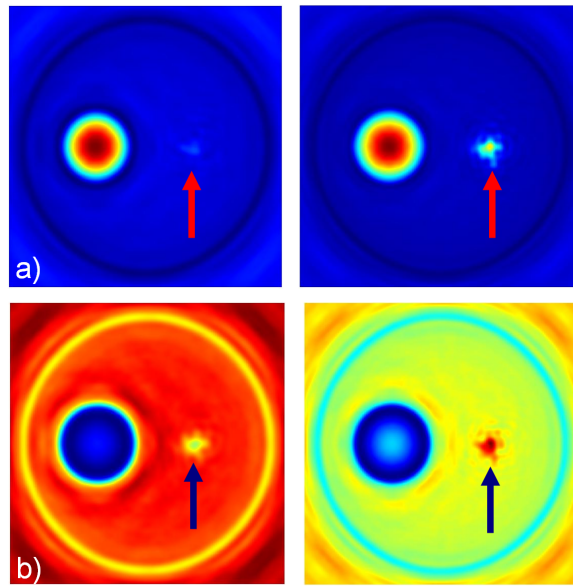
Fig. 8. OPCM images of a single cell for different values of Ψ (a: -150°, b: -90°) at RIM conditions including a cluster of 42 gold NPs at resonance (right, $\lambda = 543.0\text{nm}$) and at no-resonance (left, $\lambda = 676.4\text{nm}$). The arrows indicate the position of the cluster.
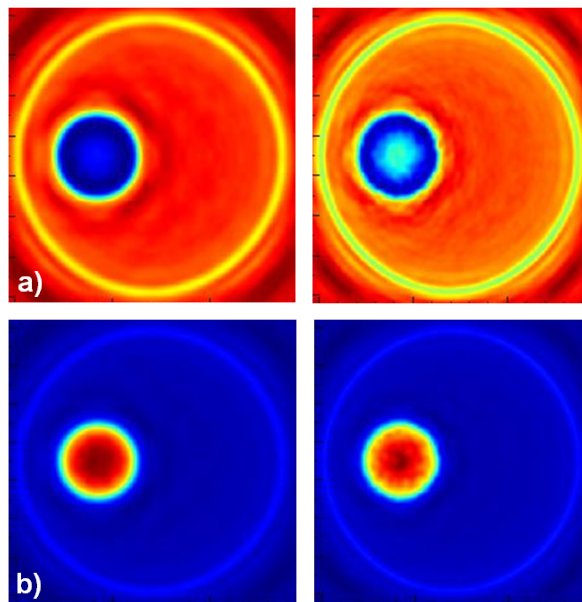

Fig. 9. OPCM images of a single cell for different values of Ψ (a: -90°, b: $+90^\circ$) at RIM conditions including 42 gold NPs randomly distributed on the surface of the nucleus at resonance (right, $\lambda = 543.0\text{nm}$) and no-resonance (left, $\lambda = 676.4\text{nm}$).

In this first scenario the specific nature of their imaging effect is determined solely by their own absorption and scattering properties. In the second scenario, when the NPs are located at the interface between the nucleus and the cytoplasm, the imaging effect of the NPs cannot be decoupled from the imaging effect of the interface which is characterized by a relatively large refractive index difference $\Delta n = 0.04$.
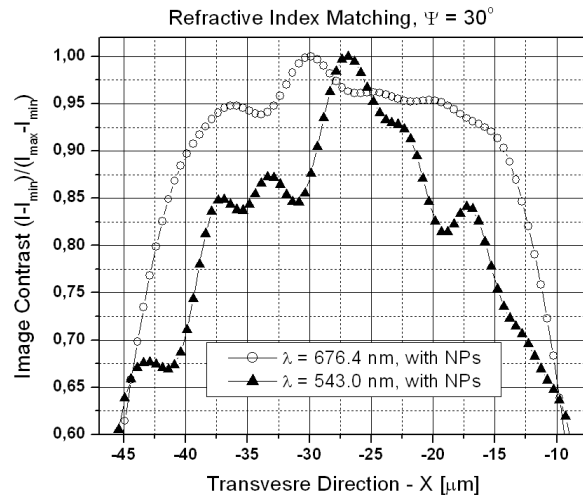
Fig. 10. Cross-sections of the cell images corresponding to the simulation scenario used in Fig. 7 and phase offset $\Psi = +30^\circ$. The specific fragmentation of the nucleus' image is due to the presence of the Gold NPs at resonant condition.

Comparing the images shown in Fig. 9 and Fig. 8 shows that the images of the cell without the gold NPs are hardly distinguishable from the images including gold NPs at no resonance conditions ($\lambda = 676.4\text{nm}$). However, the presence of the gold NPs on the surface of the nucleus at resonant conditions (see Fig. 10) can be identified by a specific fragmentation of the image of the nucleus for specific values of the offset Ψ.

5. CONCLUSIONS

In this contribution we provided a brief summary of some recent unique applications of the FDTD method for the design and modeling of nano- and biophotonics problems. The focus of the examples was on i) using SWG structures for refractive index engineering in microphotonic silicon waveguide crossings, and ii) numerically constructing OPCM images of realistic size cells to study the imaging effect gold NPs. The first example shows the ability of the FDTD approach to help in addressing a critical issue in the design and fabrication of microphotonic waveguide structures - the optimal choice for the most suitable refractive-index contrast of the waveguides. The real challenge in making this choice consists in the requirement for the refractive index values to be sufficiently high in order to guarantee a proper light confinement and, at the same time, dealing with all the consequent side effects, such as higher propagation loss, higher sensitivity to fabrication imperfections and sidewall roughness. Usually, the refractive index cannot be chosen at will but must be selected within a limited set of optical platforms. In the new design[2,3] the waveguide is longitudinally patterned with a SWG, consisting of segments of a high-refractive-index core material interlaced with a lower-refractive-index cladding material. Since the refractive-index contrast can be changed by simply controlling the grating period, SWG waveguides with different optical parameters (mode confinement, effective index, chromatic dispersion, and so on) can be realized on the same chip. This approach nicely fits the fabrication processes of planar lightwave circuits and represents a radical step forward with respect to the existing methods. The extremely low loss of the experimentally fabricated waveguides[2,3] shows that SWG waveguide applications are now able to compete with the ones based on conventional waveguides.

In what it concerns the second example, it is important to point out that in the second case all the results correspond to the case when there is a refractive index matching between the cytoplasm and the extra-cellular medium which leads to the optical clearing of the cell images. The refractive index of the extra-cellular fluid can be externally controlled by the administration of an appropriate chemical agent[11] leading to increased light transmission through cell due to the matching of the refractive indices of some of its organelles to that of the extra-cellular medium.[4-6] For example, due to optical clearing, the image contrast of the cell cytoplasm can be drastically reduced to zero levels and it is only the image of the nucleus that will remain sharply visible. Such scenario shows an unprecedented opportunity to use the optical clearing effect for the analysis of pathological changes in the eccentricity and the chromatin texture of cell nuclei within the context of OPCM configurations. This opportunity is associated with the fact that at refractive index matching

conditions the cell image is efficiently transformed into a high contrast image of the nucleus. In such conditions the imaging effect of the NPs is significantly enhanced. The presented results did not allow analyzing the scaling of the NP imaging effect as a function of the number of the NPs. However, the validation of the model provides a basis for future research in this direction.

ACKNOWLEDGMENTS

REFERENCES

[1] Dunn, A, & Richards-Kortum, R. "Three-dimensional computation of light scattering from cells," IEEE J. Selec. Top. Quant. Electr. 2, 898-894 (1996).

[2] Cheben, P., Bock, P., Schmid, J., Lapointe, J., Janz, S., Xu, D-X., Densmore, A., Delâge, A., Lamontagne, B. & Hall, T., Optics Letters 35(15), 2526-2528 (2010).

[3] Bock, P., Cheben, P., Schmid, J., Lapointe, J., Delâge, A., Xu, D-X., Janz, S., Densmore, A. & Hall, T., "Subwavelength grating crossings for silicon wire waveguides," Optics Express 18(15), 16146-16155 (2010).

[4] Tanev, S., Sun, W., Pond, P, Tuchin, V. & Zharov, V., "FDTD simulation of light interaction with cells for diagnostics and imaging in nanobiophotonics," Ch. 1 in [Handbook of Photonics for Biomedical Science], Tuchin, V., Ed., Series in Medical Physics & Biomed. Engineering, CRC Press, Taylor & Francis Ltd (2010).

[5] Tanev, S., Sun, W., Pond, P., Tuchin, V. & Zharov, V. "Flow cytometry with gold nanoparticles and their clusters as scattering contrast agents: FDTD simulation of light-cell interaction," Journal of Biophotonics 2(8-9), 505-520 (2009).

[6] Tanev, S., Pond, J., Paddon, P. & Tuchin, V., "A new 3D simulation method for the construction of optical phase contrast images of Gold nanoparticle clusters in biological cells," Advances in Optical Technologies 2008, 9 pages, doi:10.1155/2008/727418 (2008).

[7] Taflove, A & Hagness, V, Eds., [Computational Electrodynamics: The Finite-Difference Time-Domain Method], 3rd ed., Artech House, Norwood, MA (2005).

[8] Rytov, S., "Electromagnetic properties of a finely stratified medium," Sov. Phys. JETP 2, 466-475 (1956).

[9] Lalanne, P. & Hugonin, J.-P., "High-order effective-medium theory of subwavelength gratings in classical mounting: application to volume holograms," J. Opt. Soc. Am. A. 15, 1843-1851 (1998).

[10] Johnson, P. & Christy, R., "Optical constants of the noble metals," Phys. Rev. B 6, 4370-4379 (1972).

[11] Tuchin, V.V., [Optical Clearing of Tissues and Blood], PM 154, SPIE Press, Bellingham, WA (2006).